Experimental analysis of viscous and material damping in microstructures through the interferometric microscopy technique with climatic chamber

(Article begins on next page)

26 June 2024

Experimental analysis of viscous and material damping in microstructures through the interferometric microscopy technique with climatic chamber

Giorgio De Pasquale *

Department of Mechanical and Aerospace Engineering, Politecnico di Torino, Corso Duca degli Abruzzi 24, 10129 Torino, Italy

A B S T R A C T

This study describes an experimental analysis of energy dissipation due to damping sources in microstructures and micro-electromechanical systems (MEMS) components using interferometric microscopy techniques. Viscous damping caused by the surrounding air (squeeze film damping) and material damping are measured using variable geome-trical parameters of samples and under different environmental conditions. The equip-ment included a self-made climatic chamber which was used to modify the surrounding air pressure. Results show the relationship between damping coefficients and sample geometry caused by variation in airflow resistance and the relationship between quality factor and air pressure. The experimental results will provide a useful data source for validating analytic models and calibrating simulations. A thorough discussion about interferometry applied to experimental mechanics of MEMS will also contribute to the reduction of the knowledge gap between specialists in optical methods and microsystem designers.

1. Introduction

In the past two decades, a large diffusion of microstructures, related design strategies and technological building processes has been observed in a number of devices and systems addressed to many application fields. These applications, within the micro-electromechanical systems (MEMS) technology, include sensing devices (pressure sensors, inertial sensors, etc.), thermal and capacitive actuators, optical devices (mirrors, switches), transceivers, radiofrequency components (varactors, resonators, filters, etc.), biomedical microsystems and energy harvesters with more complicated layouts and efficient performances progressively emerging.

The design of microsystems is strongly complicated by the multidisciplinary competencies that involve the analysis and the modeling of crossed interactions between the microstructure and many other domains (electric, magnetic, thermal, fluidic, etc.). The study of energetic dissipations in microstructures, in particular, is one of the most crucial aspects of the design activity; a proof of this is the strong effort of researchers to formulate compact models and numerical simulations that are able to predict accurately the damping coefficients in different operating conditions. The proper control of the dissipated energy has relevant implications in the dynamic behavior, quality factor, and efficiency of the microsystem; these aspects are directly related to the sensitivity of the sensors, the precision of the actuators, the noise of the transceivers, and the efficiency and tunability of the energy harvesters, among others.

---
* Tel.: +39 0110906912; fax: +39 0110906999.
  E-mail address: giorgio.depasquale@polito.it

Despite the large variability in geometry, shape, and size of microstructures, some features, such as oscillating parts derived from the classic beam or plate, are quite common. Additionally, perforations are widely used in vibrating microcomponents because of technological process constraints (as sacrificial layer release) and to modulate fluid flows. Vibrating microstructures are subjected to viscous interactions with the surrounding fluid that is generally the primary source of energy dissipation; the environment is generally filled with air at variable pressures, although structures vibrating in liquids are also present in some applications. The air surrounding the vibrating microstructure is responsible for elastic, conservative, and viscous dissipative effects; studying the characterization of the gas flow and the forces exerted on the structure was the goal of many previous theoretical and experimental studies.

The modeling strategies developed in the literature to calculate viscous damping are based on the prediction of the fluid flow in the gaps and holes, the fluid pressure, and the elastic and dissipative fluid force components. The approaches adopted in the literature can be divided into analytic or compact [1–7] and numerical models [8–15] based on simulations of the discretized coupled-field system, for example, with FEM tools.

For measurements of damping and stiffness coefficients in microstructures, different strategies can be used [16–23]. Through the measurements of the displacement in the time domain, for instance, the decay curve of the system response to a step force directly provides the value of damping at resonance. Alternatively, the area defined by the force–displacement hysteresis curve, which is directly proportional to the energy dissipated per cycle, can be used for the damping coefficient calculation [24]. Other typologies of experimental strategies are associated with measurements in the frequency domain, such as the half-power method applied to the frequency response function (FRF) of the system at −3 dB power level with respect to the peak.

Another source of energy dissipation in microstructures is represented by the structural damping associated with the solid material of the components subjected to deformation [25–27]. These dissipations are proportional to the strain experienced by the material and are relatively high in some structural components such as elastic suspensions, linear springs, membranes, and other deformed parts. The structural damping distribution is very sensitive to the modal-deformed shape of the microstructure and the type of material. Previous works presented by the author reported experimental results of energy dissipation in terms of quality factor and damping coefficient [28,29], accompanied by the validation of results through multiphysics FEM simulations. However, the procedure adopted did not allow separating the contributions of viscous and material damping because only the global damping coefficient was detectable.

The goal of this work is to provide contributions in the experimental characterization of energy dissipation in microstructures through the optical strategy. The interferometric microscopy theory is presented from the viewpoint of microstructural analysis and is related to the conversion algorithms implemented on the most diffused microscopes. The explanation of interferometry and the influent parameters dedicated to this specific field of experimental mechanics will contribute to reduce the gap between specialists in optical methods and microsystem designers. Furthermore, the collection of experimental results in the field of MEMS damping will represent a valid source of information, for instance, for researchers needing to validate new analytic models or calibrate numerical simulations addressed to complicated geometries.

In this work, the measurement of damping in microstructures is based on the methodological approach of FRF detection in the frequency domain and the half-power method. The experimental strategy used is the optical interferometry: two light beams are pointed on the sample, and the light intensity of the interference beam is associated with a displacement coordinate by means of a dedicated conversion algorithm. The measurements at variable air pressures are conducted with an original climatic chamber that is designed and fabricated for this purpose.

The samples used are polysilicon and gold microstructures with capacitive actuation, including a perforated membrane with variable shapes and sizes, supported by four beams working as elastic suspensions; the dimensions of the samples are treated as parametric variables to investigate their influence on the damping coefficient variation. For the tests in the climatic chamber, the samples are preliminarily subjected to the wire-bonding process to permit electric supply of microstructures. Differently from previous works of the author, the present measurements at low air pressure allow reduction of the contribution of viscous damping and accurate estimation of the dissipations associated with damping inside the material.

2. Experimental methodology

The experimental characterization of the microstructure dynamic response is the preliminary step of the damping measurement. For tests at low air pressure conditions, the climatic chamber described in the next sections is used; this measurement methodology was able to detect the position of the sample situated inside the chamber from the outside through a special optically compensated glass, allowing complete contactless detection.

Optical detection strategies offer many advantages for investigating MEMS dynamics. These strategies provide a large measurement field suitable for millimeter-sized structures accompanied by high spatial resolution. They preserve device integrity because of the contactless nature of measurement (even sample heating can be prevented by using low-power density of the light source); then, optical measurements allow both static detections for evaluating 1D, 2D, and 3D profiles and dynamic detections for capturing modal shapes and vibration spectra. Finally, optical methods can be applied directly on the sample surface without preliminary treatments and have low sensitivity to environmental disturbances like temperature floating or airflows. Furthermore, contactless measures are necessary when using electrical probes to supply

the devices, or the detection must be conducted through the glass of a climatic chamber. These cases require additional special long-distance objectives [30].

In static analyses, optical techniques are generally divided into two groups: techniques based on single-point detection combined with the translation of the detector (scanning-point profilometers) and techniques based on detector arrays for simultaneous measurement of many points (full-field profilometers), which are more suitable for 3D profiling. Microscopic interferometry allows vertical resolution down to 0.1 nm and lateral resolution in the submicron range [31]. Most of the drawbacks of interferometric techniques (limited detectable step height, material reflection properties, and limitation of vertical range imposed by objective depth of focus) can be easily overcome by using white light instead of monochromatic light: multiple wavelengths can be optically separated to perform parallel detections with improved measurement range and disturbance insensitivity. Furthermore, the influence of mechanical drift on the measurement can be drastically reduced by fast detections based on phase modulation. The full-field detection using interferometry is available through overlapping techniques consisting in merging several portions of the profile to obtain a large full image of the specimen.

Alternative full-field techniques are widely used in mechanical engineering, such as holographic interferometry, digital holography (DH), and electronic speckle pattern interferometry (ESPI); in these cases, however, the interference is generated from the light reflected or scattered by the sample surface, and a minimum value of the roughness is needed to get the required sensitivity threshold. Unfortunately, in MEMS structures, most surfaces are smooth, and the intensity of scattered light is too weak, suggesting that the application of these strategies is limited to few cases.

In dynamic measurement field, the microscopic interferometry detects the sample vibration from the variation of the contrast among interference fringes and offers relevant advantages [32–34]. For instance, it allows full-field target detection, provides considerably high resolution of detectable displacement (less than 1 nm), and allows fast detection of vibration spectra by sweeping actuation frequency. Other strategies are available, among which, laser Doppler and laser deflection are the most diffused; the first one measures the phase (or the optical frequency) shift induced by the Doppler effect on the light beam reflected by the sample surface, and the last one measures the angular variation of the same reflected beam during sample vibration. Although these approaches are well established in MEMS and widely used in this field, they have some drawbacks: laser Doppler requires considerable time consumption to perform the complete surface scanning, and the laser deflection method exhibits strong sensitivity between the detected displacement and the local slope variation. In addition, it requires complicated setups with high-aperture optics for focusing and detecting the reflected spot.

For the reasons mentioned, optical interferometry was selected for this experimental investigation and especially because of the suitability for dynamic out-of-plane measurements, the high sensitivity (in the order of light wavelength), the insensitivity to mechanical drift and environmental disturbances, and the possibility of implementing automatic scanning with considerable shortening of detection time.

2.1. Optical interferometry applied to microstructures

Two light beams are directed to the same point of the sample surface, and an interference light beam is produced. The intensity of the interference light beam depends on the phase shift between the two original beams at the time of collision, which is the function of their paths. The optical interferometric experimental technique is based on the possibility of converting the intensity of the interference light to the optical path difference (OPD) between the two original beams (namely, the arms of the interferometer) and, finally, to the position of the target point, corresponding to the sample surface.

By considering the two light wave sources described by the following equations:

$$E_1 = E_{10} \sin(\omega t - \varphi_1) \tag{1}$$

$$E_2 = E_{20} \sin(\omega t - \varphi_2), \tag{2}$$

the optical interference generates the wave:

$$E = E_0 \sin(\omega t - \vartheta), \tag{3}$$

where E_i is the oscillation amplitude, φ_i is the phase angle of source beams at the interference point, θ is the phase angle of the interference beam, and ω is the angular frequency. Through simple calculations, the following relation between the amplitudes of the interference wave and the original light waves is obtained:

$$E_0 = \sqrt{E_{10}^2 + E_{20}^2 + 2E_{10}E_{20}\cos(\varphi_1 - \varphi_2)} \tag{4}$$

This shows that the interference wave amplitude depends on the phase difference between the source waves at the interference point. The theoretical equation expressing the phase angle of interference beam as function of the phase angles of the source beams is

$$\vartheta = \arctan\left(\frac{E_{10}\sin\varphi_1 + E_{20}\sin\varphi_2}{E_{10}\cos\varphi_1 + E_{20}\cos\varphi_2}\right). \tag{5}$$

The optical interference can be generated only from the interaction of coherent light beams; usually, in traditional optical devices, it is generated by the same source to provide them the same frequency. A simple application of light interference to measurements is schematically represented in Fig. 1. The light wave coming from source (1) is separated into two beams (2, 3)
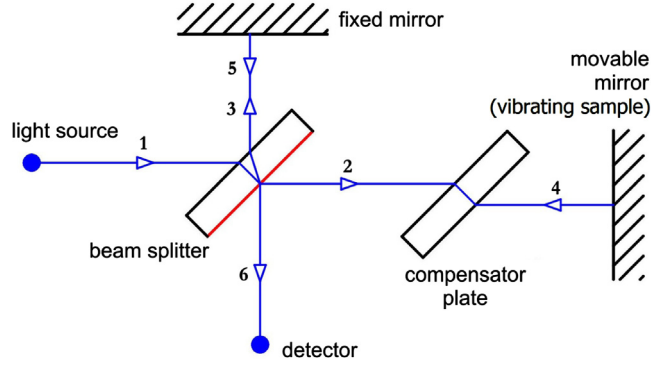
Fig. 1. Optical interferometer working principle.

by the beam splitter (e.g., a half-silvered mirror) and directed to a couple of separate mirrors. After reflection, the beams (4, 5) rejoin themselves prior to being captured by a detector (6). One of the mirrors is movable and allows varying the travel length of the corresponding light beam, producing an OPD between the two arms of the interferometer. The reported scheme also includes a compensator plate: the beam splitter causes a variation of the light travel length on the first arm of the interferometer because of refractive effects. Thus, it is necessary to induce the same variation on the second arm to preserve the coherence between light beams. This function is carried out by the compensator plate that, having the same optical and geometrical properties of the splitter, replicates the same light refractions even on the second arm.

The quantitative detection of light waves can be performed by many different light sensors (e.g., photocells) that commonly are able to read its intensity, making this parameter relevant for interferometric techniques. In the case of source light beams with the same amplitude ($E_{10} = E_{20}$), the light intensity $I = E_{i0}^2$ of the interference beam can be derived directly from Eq. (4). Considering the relation $\Delta\varphi = (2\pi\Delta x)/\lambda$ between the phase shift and the OPD (see Appendix A), the light intensity is expressed by the following equation:

$$I = 4E_{i0}^2 \cos^2\left(\frac{\pi\,\Delta x}{\lambda}\right), \tag{6}$$

where λ is the wavelength, and Δx is the OPD between the sources. In this condition, from Eq. (5), the following can be easily derived: $\theta = (\varphi_1 + \varphi_2)/2$.

The averaged expression of the light intensity resulting from Eq. (6) is calculated on the time interval needed to cover the travel Δx (i.e., the OPD) by the surface of the vibrating sample. This interval is many times shorter than the oscillation period, and the OPD is many times smaller than the sample oscillation amplitude. This assures the desired sensitivity on the evaluation of displacement through the measurement of the light intensity by the detector.

Eq. (6) describes the basic function of the measurement devices having the optical interference as the working principle; the common solution is to keep one the mirrors constant and correlate the other one with the sample surface. When the specimen is moving, the intensity of the interference wave varies according to the amount of the displacement; alternatively, when the specimen surface is affected by profile irregularities, for instance, because of superficial roughness or shape topology, the interference light intensity varies along the surface.

The light intensity is measured by the detector; in the actual setting, it is represented by a charge-coupled device (CCD) camera, and the image resolution is increased by coupling a microscope to the interferometer.

The microscope coupled to the interferometer has the effect of introducing a magnification of the captured image, which must be included in the conversion algorithm. By introducing a couple of coordinates x,y to identify each point (or pixel) on the detector surface and the magnification factor G of the microscope, Eq. (6) can be written in the final form (see Appendix A)

$$I(x,y) = I_{\text{amb}}\left(\frac{x}{G},\frac{y}{G}\right)\left[1 + C\left(\frac{x}{G},\frac{y}{G},\Delta x\right)\cos\left\{\frac{4\pi\,\Delta x((x/G),(y/G))}{\lambda_m(1+f)} + \varphi_2\left(\frac{x}{G},\frac{y}{G}\right) - \varphi_1\right\}\right], \tag{7}$$

where I_{amb} is the ambient light intensity, (x/G, y/G) are the coordinates of the specimen surface corrected with the magnification of the microscope, and f is the correction factor dependent on the objective aperture. The wavelength λ has been changed to λ_m representing the average wavelength of the light spectrum because, generally, it is not possible to detect a perfectly monochromatic light beam in real conditions. The coefficient

$$C = \frac{I_{\text{amb}} - I_{\text{min}}}{I_{\text{amb}}} \tag{8}$$

represents the fringe contrast, where I_{min} is the minimum light intensity.

The period of the reported function, corresponding to the period of interferometric fringes, is

$$T = \frac{\lambda_m(1+f)}{2}. \tag{9}$$

The values of the variables I_{amb}, C, φ_2, and Δx are dependent on the position on the sample surface and are influenced by the inhomogeneity of the ambient light and the optical properties of surface materials. Therefore, the value of C can be influenced by the OPD if shape discontinuities of the surface are comparable to the microscopic depth of field or to the coherence length of the light source.

In the dynamic tests needed for evaluating the damping coefficients, the sample is subjected to alternate motion; in this case, the OPD is defined as a function of the specimen surface displacement as described in Appendix A. Common light sensors are able to measure the light intensity on each pixel as the average over a determined time interval T_0 (usually some centimes of a second). This average intensity I_m can be expressed with the integral of the dynamic light intensity (Eq. (A20)) over the time T_0 divided by the same time interval, giving the following equation:

$$I_m(x,y) = I_{amb}\left[1 + C(\Delta x_0)J_0\left(\frac{4\pi a}{\lambda_{ma}}\right)\cos\left(\frac{4\pi \Delta x_0}{\lambda_{ma}} + \Delta\varphi\right)\right], \tag{10}$$

where Δx_0 is the average position of the sample, a is the amplitude of oscillation, and J_0 is the 0-order Bessel function containing information about the displacement of the sample. Eq. (10) represents the algorithm used by the microscope to convert the light intensity detected by the light sensor to the sample dynamic displacement. This conversion equation is suitable to measure the real-time FRF of the system under analysis [33,34]. From Eq. (10), it is seen that the maximum difference between the measured light intensity and the ambient light intensity is reached when the equation is

$$\cos(4\pi\Delta x_0/\lambda_{ma} + \Delta\varphi) = \pm 1. \tag{11}$$

This consideration is useful to set properly the experimental measurements: by calibrating the sample static position, interference fringes having the maximum and the minimum values of intensity can be obtained in dynamic conditions; the described procedure increases the contrast between two adjacent fringes and improves the resolution of the measurement.

2.2. Half-power method for damping estimation

The algorithm described in the previous section is applied to the interferometric microscope for converting the light intensity measured on the sample surface to oscillation amplitude when a sinusoidal excitation force is applied. The detection camera points on a few pixels and registers the light intensity variation during the oscillation cycle; after the conversion, the oscillation amplitude is obtained and stored. The same measurement is repeated at variable frequencies of excitation within a certain range that includes the sample resonance (sine sweep); finally, the FRF is obtained by plotting the sequence of measured amplitudes.

The half-power method is used to calculate the global damping coefficient of the microstructure from the experimental FRF. First, the measured response function in the frequency domain is interpolated by means of the sixth-order polynomial $h(f)$; the maximum value of the function is then determined and used to compute the half-power level of the microstructure response corresponding to –3 dB decay from the peak. The half-power is

$$[h(f)]_{-3\text{ dB}} = \frac{\max[h(f)]}{\sqrt{2}}. \tag{12}$$

Corresponding to the half-power level, the two half-power frequencies, namely, f^{I} and f^{II}, are identified as represented in Fig. 2. They define the half-power bandwidth expressed by the following equation:

$$\Delta f = f^{\mathrm{II}} - f^{\mathrm{I}} = 2\zeta f_n, \tag{13}$$

where ζ is the global damping ratio and f_n is the resonance frequency. FRF refers to the vibrating microstructures under the influence of the surrounding air and material dissipations; thus, the measured damping includes both viscous and structural
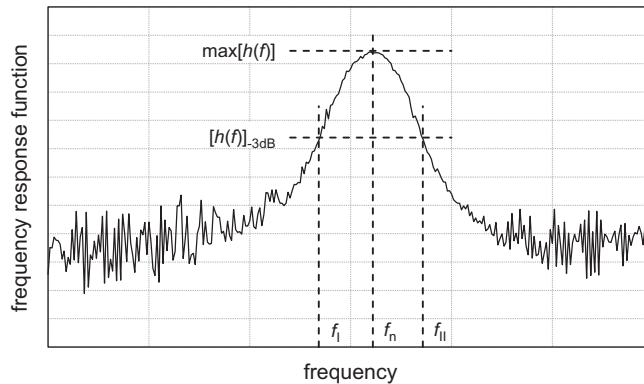

Fig. 2. Half-power method applied to the FRF.

components. The experimental quality factor of the microstructure can be estimated as

$$Q = \frac{f_n}{\Delta f}. \tag{14}$$

Both the half-power bandwidth and the resonance frequency can be measured directly on the FRF; therefore, the damping ratio and the quality factor are easily obtained from Eqs. (13) and (14), respectively.

Then, the damping coefficient can be calculated by the following equation:

$$c = 2m\zeta(2\pi f_n), \tag{15}$$

where m is the modal mass participating in the resonance considered. For the samples used in this work, the modal mass can be approximated to the mass of the central plate. Alternatively, for more complicated geometries, the exact value of the modal mass can be estimated, for instance, by using a finite element method (FEM) numerical model. Furthermore, this method also allows the estimation of the global dynamic stiffness of the microstructure by the simple relation:

$$k = m(2\pi f_n)^2. \tag{16}$$

Alternative methods can be used for extracting the damping coefficient, for instance, by measuring the phase shift between the actuation force and the displacement response of the structure; in this case, measurements in the time domain are needed, and the cited parameters must be measured simultaneously. Instead, the method used in this study considers the experimental results coming directly from the optical measurement, which are the amplitude of resonance peak measured in the frequency domain and its attenuated value (half-power).

3. Experimental instrumentation

3.1. Climatic chamber design and building

The climatic chamber represented in Fig. 3 has been designed and fabricated to conduct the measurements at low air pressures. The central cylindrical base and the cover of the chamber are made of steel; the adhesion of the cover is assured by six screws and a rubber seal. The dimensions of the internal volume are 80 mm (base diameter) and 76 mm (height), and the thickness of the lateral wall is 35 mm. The high thickness of the wall and the base can increase the mass of the chamber to reduce the effects of vibrations generated by the vacuum pump. A movable stage (diameter, 43 mm) that is able to translate in the vertical direction and tilt is provided in the chamber; it is supported by four elastic springs and is used to support and orient the samples. The tilting angle of the stage can be varied through the rotation of the regulation screws. A glass plate (diameter, 35 mm; thickness, 1.75 mm) that is compensated for the interferometric microscope is situated at the center of the cover to allow the optical detection of samples with the microscope objective situated outside the chamber. The climatic chamber is equipped with four pipe connections DN40, which are used to connect the vacuum pump, pressure sensor, microflow leak valve, and DB9 port (Fig. 4a) for the electric supply of samples. The vacuum pump Alcatel Drytel 1025 AS has been used; it is based on two separate stages: an alternative membrane pump for the low vacuum and a turbomolecular pump for the high vacuum (7.5 l/s nominal flow rate, 10^3–10^{-6} mbar pressure range). The pump is connected to the chamber through a 1-m-long flexible pipe that is able to dissipate the vibrations. A manual gate valve (VAT 01.2) has been added to the chamber inlet to isolate its internal volume from the flexible pipe when the pump is turned off.

The pressure level in the chamber can be adjusted by acting on a microflow leak valve (1×10^9 mbar l/s tightness) that introduces a very small regulated airflow from the ambient.

The climatic chamber has been designed also for controlling the temperature of the microstructures under investigation; this is possible through a Peltier cell situated on the internal movable stage and supplied by a DC voltage. The temperature can be varied within the range −20 to 100 °C. A PT100 temperature sensor is situated on the Peltier cell to provide the feedback signal for the temperature control (Fig. 4b).
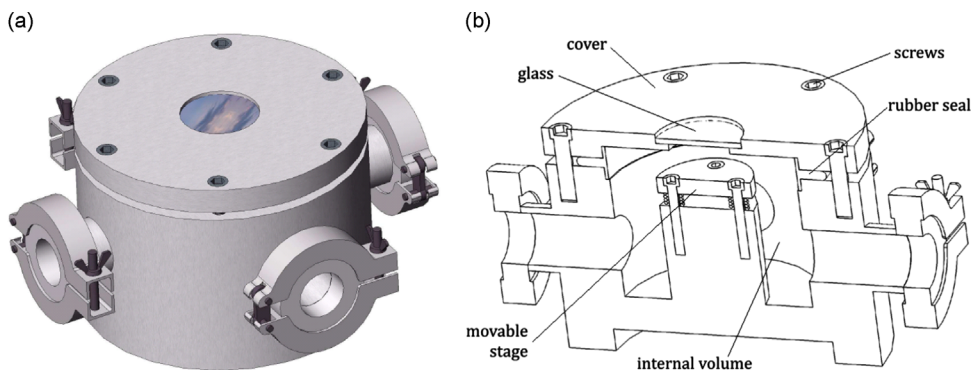
(a) (b)

Fig. 3. Climatic chamber for tests in environments with controlled pressure and temperature: 3D drawing (a) and cross-section schematics (b).
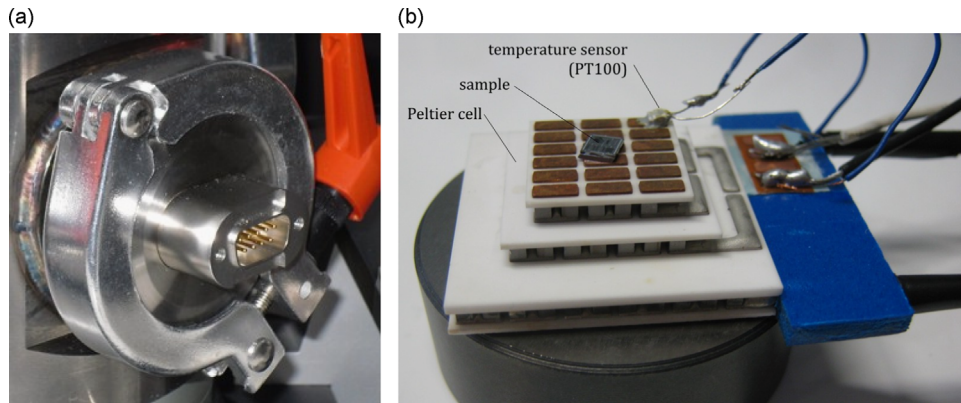
Fig. 4. DB9 port for electric supply of microstructures and devices inside the chamber (a) and Peltier cell with a PT100 temperature sensor (b).
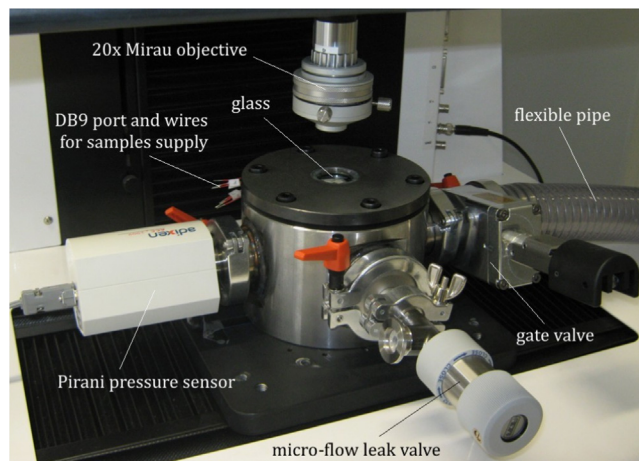

Fig. 5. Complete experimental setup, including vacuum chamber, airflow controllers, voltage supply, and interferometric microscope.

The electric supply is provided to the samples by wires through the DB9 port. The same DB9 port is used to supply the Peltier cell and the PT100 temperature sensor when they are used for the tests. The pressure sensor Pirani-Penning ACC2009 (10^3–5×10^{-9} mbar measurement range, 30 percent accuracy, 5 percent repeatability) is used to control the air pressure inside the chamber. The complete experimental setup for environmental controlled tests is reported in Fig. 5, where the climatic chamber, microscope Mirau objective, pressure sensor, samples' electric supply, airflow valves, and flexible pipe connected to the pump are visible.

3.2. The interferometric microscope

The measurements are conducted with the interferometric microscope ZoomSurf 3D (Fogale Nanotech). The conversion algorithm described in Section 2.1 can be used for static and dynamic tests. In the first case, the instrument works as an optical profilometer; the surface of many different materials (metals; polymers; semiconductors; biological; thin transparent layers such as varnishes, plastics, and glasses; etc.) can be analyzed also by merging several detections. Statistical analyses of surface roughness can be performed, and by means of the software for image processing, the quasi-static deformation of samples is measured through a series of successive detections. In case of dynamic tests, the microscope is suitable for measuring the real-time FRF of microstructures and detecting the modal deformed shape by means of stroboscopic light; in this last case, a series of successive images of the deformed sample are captured and then used to reproduce the modal displacements at low velocity.

For dynamic measurements, the red monochromatic light source is preferred to generate interferometric fringes with variable light intensity and constant amplitude. The measurement of the phase shifting of interference fringes is the basic principle of the technique called "phase shifting interferometry," which allows rapid measurements of microstructures in motion, as well as etching controls, micromachining processes monitoring, and optical component characterization. Because of its intrinsic incoherent nature, the polychromatic white light source determines the rapid decay of fringe intensity and thickness. The "white light interferometry" technique is based on the localization of the maximum fringe contrast area and is used for the static superficial profile measurements of large and irregular components.

The optics mounted on the microscope are able to perform profile measurements from a minimum area of $100 \times 100\ \mu m^2$ to a maximum area of $2 \times 2\ mm^2$. The setting used in the measurements includes the Mirau objective with $20\times$ magnification factor that provides 0.6 μm lateral and 0.1 nm vertical resolutions. The maximum detectable height difference (i.e., the thickness of vertical steps) in a single measurement is 400 μm; the samples are situated on a stage that is electrically moved in the x,y plane and is able to support a maximum weight of 5 kg. The same stage is used to host the climatic chamber when measurements in a controlled environment are performed. The objective moves along the z-axis and can cover the distance of 250 mm. The stage slope can be changed by means of mechanical screws to adjust the orientation and the thickness of fringes. Through the software, it is possible to modify some optical parameters such as the objective magnification factor (G) and the reflection coefficient of the reference mirror. A dedicated function allows recognition of the portions of the specimen that are excessively sloped and the parts covered by a layer of dust and excludes them from the evaluation. The excitation voltage for dynamic tests is provided by the embedded generator in the range of 0–200 V at frequencies of up to 2 MHz.

In case of measurements with the climatic chamber, the special $20\times$ LWD Mirau objective (0.28 numerical aperture, 12.5 mm working distance) is used; this objective allows the manual compensation of the presence of the additional glass situated on top of the chamber that modifies the optical paths along the two arms of the interferometer. The compensation is necessary to produce the optical interference (and the interference fringes) on the sample surface situated inside the climatic chamber.

4. Microstructure samples

The samples of the microstructures are represented by a central plate with square holes and four lateral supporting springs. Shape, size, and material are variable among the samples; they can be divided into two types: square plates made with electroplated gold and rectangular plates made with electroplated gold or polysilicon. The microstructures are
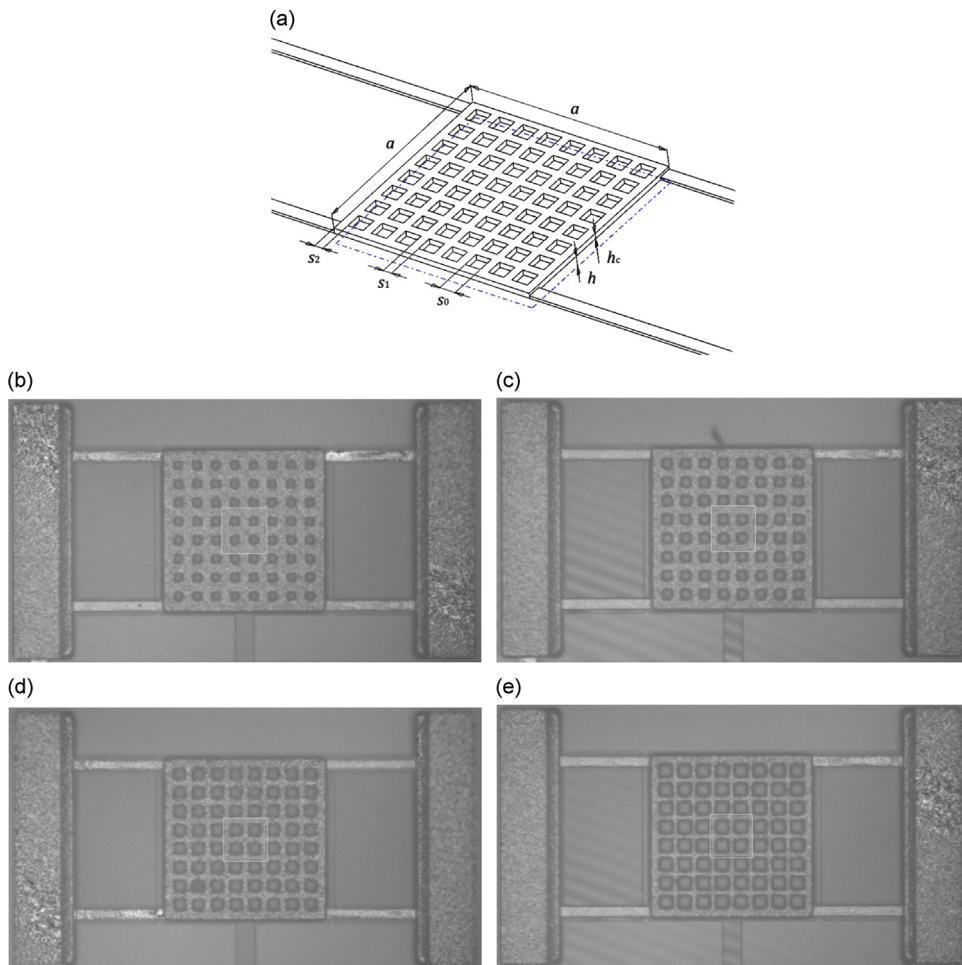

Fig. 6. Square plate samples (typology I): geometrical parameters (a) and optical image of samples I.25 (b), I.26 (c), I.27 (d), and I.28 (e). The active window reference for the optical detection of displacement is reported at the center of each structure.

actuated by an electrostatic force in the vertical out-of-plane direction through the counterelectrode situated on the substrate below the suspended plate. The nominal material properties of electroplated gold and polysilicon are as follows: Young's modulus E_g=98.5 GPa, and E_p=147 GPa; Poisson's ratios ν_g=0.42, and ν_p=0.21; densities ρ_g=19.32 $\times$ 10^{-15} kg/μm^3, and ρ_p=2 $\times$ 10^{-15} kg/μm^3.

The square plates (typology I) have the geometry introduced in [14] and reported in Fig. 6a. The plate-side length (a), the hole-side length (s_0), and the number of holes ($M \times M$) are the variable parameters; the nominal thickness of the plate is h_c=6.3 μm, and the air gap height is h=3.0 μm. The average measured length (L_B) and width (W_B) of the supporting springs are 96.66 and 12.88 μm, respectively, and their average thickness is 2.606 μm. The optical images of some samples (I.25–I.28) belonging to typology I are shown in Fig. 6b–e, where the hole size parameter variation is clearly visible among the variants and where the active window for the optical detection of displacement is reported.

The dimensions of the samples (typology I) are reported in Table 1, together with the total number of holes, $M \times M$. The dimensions indicated have been measured by a microscope with the static interferometric technique; the tolerances of the reported values correspond to the sensitivity error given by the microscope resolution (horizontal, 0.6 μm; vertical, 0.1 nm). The distance between two adjacent holes (s_1) and that between the peripheral holes and the plate border (s_2) can be calculated with the following relations:

$$s_i = \frac{a}{M+1} - \frac{s_0}{i}, \quad i = 1, 2 \tag{17}$$

The geometry of rectangular plate samples (typology II) built in gold and polysilicon was introduced in [28,29], respectively. The nominal plate thicknesses h_c of gold and polysilicon microstructures are 6.3 and 15 μm, respectively, and the nominal air gap thicknesses h are 3 and 1.6 μm, respectively.

The geometry and shape of samples belonging to typology II are represented in Fig. 7a, and the optical images of gold and polysilicon microstructures are also reported (Fig. 7b and c). These images also include the active window for the optical detection of displacement.

The dimensions of samples (typology II) are listed in Table 2, and the number of holes present along the longer (M) and the shorter (N) sides of the plate is also indicated. The average measured dimensions of the supporting beams are L_B=96.08 μm (length), W_B=13.52 μm (width), and 2.620 μm (thickness) for rectangular gold structures and L_B=122.90 μm (length), W_B=3.92 μm (width), and 15.063 μm (thickness) for polysilicon structures. The dimensions indicated have been measured by a microscope with the static interferometric technique and are affected by the tolerances previously reported. The distance between two adjacent holes (s_1) and the distance between the peripheral holes and the plate border (s_2) can be

Table 1
Dimensions of samples with gold square plate (typology I).

| Sample	Plate side a [μm]	Holes side s_0 [μm]	Number of holes $M \times M$	Plate thickness h_c [μm]
I.1	55.91	7.20	4	6.297
I.2	55.07	9.31		6.291
I.3	55.70	10.70		6.302
I.4	55.89	12.59		6.322
I.5	76.25	7.18	9	6.311
I.6	76.40	9.29		6.303
I.7	76.47	10.68		6.311
I.8	76.41	12.62		6.299
I.9	96.45	7.21	16	6.309
I.10	96.51	9.31		6.298
I.11	96.33	10.68		6.307
I.12	96.12	12.61		6.296
I.13	115.47	7.21	25	6.304
I.14	115.42	9.31		6.275
I.15	115.39	10.71		6.298
I.16	115.74	12.60		6.302
I.17	137.14	7.21	36	6.307
I.18	137.08	9.31		6.296
I.19	137.13	10.68		6.332
I.20	137.11	12.61		6.286
I.21	157.31	7.18	49	6.303
I.22	157.28	9.29		6.278
I.23	157.63	10.69		6.285
I.24	157.13	12.59		6.285
I.25	185.96	7.19	64	6.312
I.26	185.28	9.33		6.321
I.27	185.97	10.70		6.287
I.28	185.13	12.58		6.297
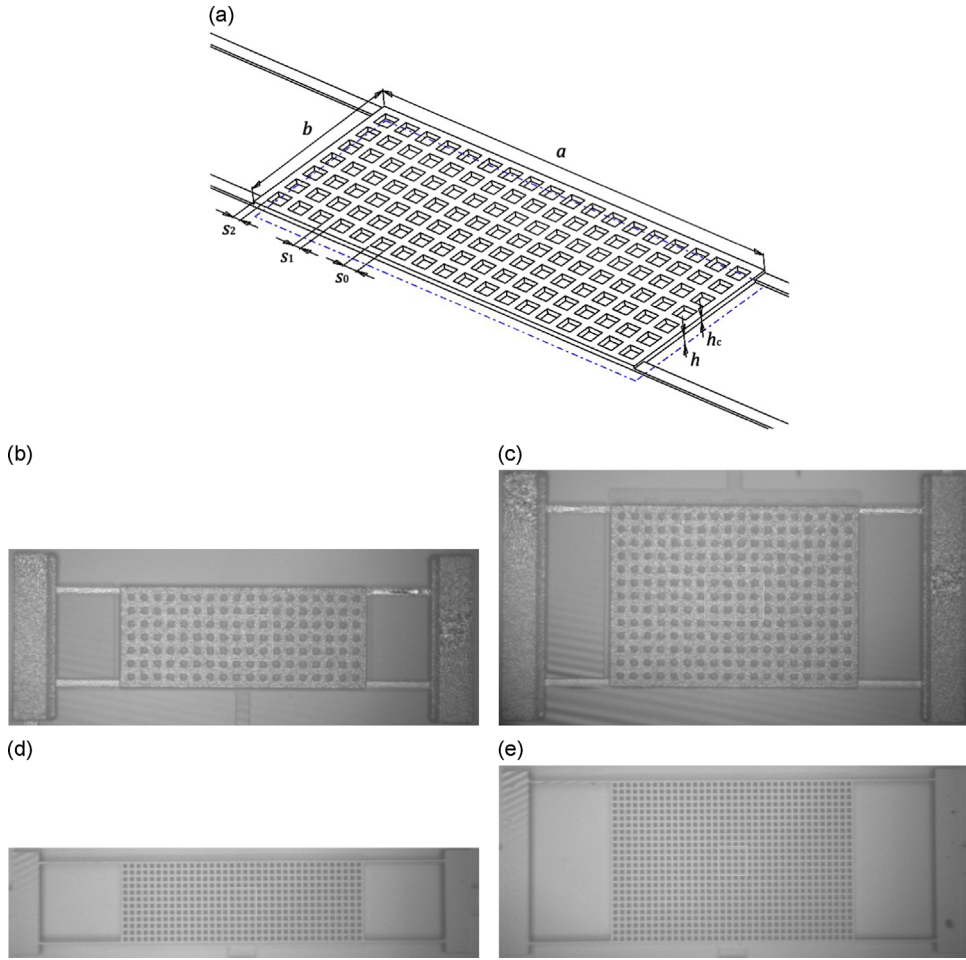
Fig. 7. Rectangular plate samples (typology II): geometrical parameters (a) and optical image of gold II.5 (b) and II.6 (c) and polysilicon II.11 (d) and II.12 (e) variants. The active window reference for the optical detection of displacement is reported at the center of each structure.

Table 2
Dimensions of samples with gold and polysilicon rectangular plate (typology II).

Sample	Plate length a [μm]	Plate width b [μm]	Holes side s_0 [μm]	Number of holes $M \times N$	Plate thickness h_c [μm]
Gold samples					
II.1	376.13	96.66	7.21	18 × 4	6.298
II.2	376.47	96.50	9.29	18 × 4	6.303
II.3	376.81	96.63	10.69	18 × 4	6.257
II.4	376.47	96.61	12.60	18 × 4	6.323
II.5	376.44	156.94	7.21	18 × 7	6.302
II.6	376.13	276.98	7.20	18 × 13	6.312
Polysilicon samples					
II.7	372.4	66.4	5.0	36 × 6	15.012
II.8	363.9	63.9	6.1	36 × 6	15.023
II.9	373.8	64.8	7.3	36 × 6	14.972
II.10	369.5	64.5	7.9	36 × 6	15.003
II.11	363.8	123.8	6.2	36 × 12	14.989
II.12	363.8	243.8	6.2	36 × 24	15.006

calculated using Eq. (17) or the following relations, written for the short side of the plate:

$$s_i = \frac{b}{N+1} - \frac{s_0}{i}, \quad i = 1, 2 \tag{18}$$

According to the results of previous studies [35], the first deformed shape of all the samples tested consists of the flexural deflection of lateral springs and the quasi-rigid displacement of the central plate in the vertical direction. The microfabrication
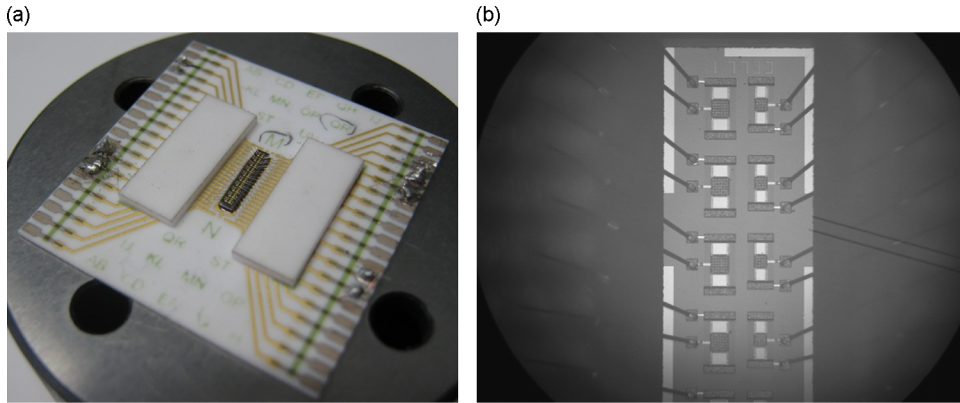
Fig. 8. Wire-bonded samples for tests into the climatic chamber: bonded dice (a) and microscopic detail of wires bonded on gold pads (b).

tolerances affecting the geometrical dimensions of the samples may induce small tilting angles of the plate during oscillation. However, the modeling of air damping by means of analytical models presented in [29], which assumes uniform air gap thickness, provided results in good agreement with experiments, suggesting that tilting angles of the plate are negligible. The structural displacement in the time domain when the samples are subjected to alternate voltage supply is almost perfectly sinusoidal, as confirmed by the measurements conducted with the laser Doppler technique in [36] on the same structures. This property of the samples confirms the applicability of the measurement setting described and the effectiveness of the method used to process the experimental data.

For tests at ambient air pressure, the microstructures are supplied with conductive probes applied to the square contact pads situated near the samples and visible in the reported images. For tests at low air pressure, the electric actuation is carried into the climatic chamber by means of electric wires passing through the DB9 port and connected to the samples, which are previously subjected to the wire-bonding process, as shown in Fig. 8.

5. Results

5.1. Air damping at ambient pressure

The results of experimental measurements of resonance frequency, half-power bandwidth, damping coefficients, and damping ratio are listed in Tables 3 and 4 for the samples of typologies I (square plates) and II (rectangular plates), respectively, at ambient air pressure conditions.

Two types of errors affect the measured values of damping coefficients and quality factor; the errors are related to the experimental procedure used and the microscope resolution. The first source of error depends on the frequency step of the discretized sine sweep used to excite the microstructure. The second source of error is related to the sensitivity of the interferometric microscope in the vertical direction for the evaluation of the out-of-plane dynamic oscillation amplitude.

Some experimental FRFs are presented in Fig. 9 as examples. The measured resonance frequencies are reported in Fig. 10 for the gold and the polysilicon microstructures; the influence of plate-side length and hole dimensions on resonance frequency is clearly shown in Figs. 11 and 12.

5.2. Air damping at low pressure

The damping coefficient of test structure I.17, which belongs to typology I (gold square plates), has been measured at variable air pressures by means of the climatic chamber. The experimental methodology applied is the same as the one previously described for the tests at ambient pressure, and the measurement error analysis and the settings of sine sweep excitation are still valid. Through the climatic chamber, the measures have been performed at static air pressures variable from the ambient pressure down to 1.26 mbar, corresponding to low vacuum conditions. The results are listed in Table 5. As a consequence of air rarefaction, the viscous dissipations of air are reduced, and the resonance peak becomes sharper as the pressure lowers. The changes in dynamic response are also proven by the quality factor increase and the half-power bandwidth (Δf_n) reduction accompanying the pressure drop. The dynamic response variation due to the different air pressures of the environment is shown in Fig. 13, which displays the FRF of sample I.17 when the pressure is progressively reduced. The sharpness of the resonance peak increases considerably at low pressures, indicating the lower influence of viscous damping. The variations of the damping coefficient and the quality factor are reported in Fig. 14. The results show that reducing the pressure from ambient to 1.26 mbar increases the quality factor by about 10 times. The interpolation of the experimental results shows the asymptotic trend of the damping coefficient for low pressures. The residual damping at the lowest pressures is the component of dissipations depending on the material and on the structure itself (anchor losses,

Table 3
Measured values of resonance frequency, half-power bandwidth, damping coefficient, and damping ratio ($100\times$) of samples with gold square plate (typology I).

Sample	Resonance frequency f_n [kHz]	Half-power bandwidth Δf [kHz]	Plate mass m [kg 10^{-10}]	Damping coefficient c [N s 10^{-6}/m]	Damping ratio ζ [%]
I.1	71.04	0.7389	3.551	1.648	0.520
I.2	74.54	0.7143	3.265	1.465	0.479
I.3	76.67	0.4998	3.220	1.011	0.326
I.4	79.21	0.3984	3.041	0.761	0.251
I.5	58.16	0.6172	6.523	2.530	0.531
I.6	59.65	0.6103	6.162	2.363	0.512
I.7	61.57	0.5264	5.878	1.944	0.427
I.8	63.58	0.3888	5.361	1.310	0.306
I.9	47.78	0.8296	10.325	5.382	0.868
I.10	48.76	0.6486	9.646	3.931	0.665
I.11	50.69	0.5260	9.083	3.002	0.519
I.12	54.06	0.5487	8.144	2.808	0.508
I.13	41.27	0.8823	14.656	8.125	1.069
I.14	42.28	0.6353	13.523	5.398	0.702
I.15	43.80	0.5170	12.712	4.129	0.590
I.16	45.66	0.5607	11.478	4.044	0.614
I.17	34.17	0.7733	20.637	10.027	1.131
I.18	35.03	0.5770	19.062	6.911	0.824
I.19	36.61	0.5239	17.981	5.919	0.716
I.20	39.72	0.5541	15.879	5.528	0.698
I.21	29.82	0.8886	27.059	15.107	1.490
I.22	29.86	0.6305	24.874	9.854	1.056
I.23	31.00	0.5939	23.372	8.721	0.958
I.24	33.60	0.5833	20.549	7.531	0.868
I.25	22.04	0.7785	38.136	18.654	1.766
I.26	25.36	0.5913	35.119	13.048	1.166
I.27	26.28	0.5592	33.108	11.633	1.064
I.28	28.13	0.5584	29.374	10.306	0.992

Table 4
Measured values of resonance frequency, half-power bandwidth, damping coefficient, and damping ratio ($100\times$) of samples with gold and polysilicon rectangular plate (typology II).

Sample	Resonance frequency f_n [kHz]	Half-power bandwidth Δf [kHz]	Plate mass m [kg 10^{-10}]	Damping coefficient c [N s 10^{-6}/m]	Damping ratio ζ [%]
Gold samples					
II.1	20.25	1.1278	39.684	28.121	2.786
II.2	20.70	0.8652	36.673	19.936	2.090
II.3	20.98	0.5022	34.069	10.750	1.197
II.4	21.92	0.3847	30.467	7.364	0.878
II.5	17.00	1.2793	63.956	51.408	3.762
II.6	13.61	2.3788	112.253	167.778	8.741
Polysilicon samples					
II.7	201.64	11.037	5.803	40.241	0.173
II.8	204.33	5.728	4.572	16.454	0.139
II.9	211.01	3.490	3.806	8.347	0.119
II.10	222.28	3.397	3.106	6.630	0.100
II.11	173.90	6.071	8.523	32.513	0.219
II.12	138.56	5.496	16.651	57.501	0.340

thermoelastic damping, etc.), and it is almost independent of the viscous dissipations of air, the amount of which is given by rarefied gas theories.

5.3. Experimental uncertainty

Two types of errors affect the measured values of damping coefficient; they depend on the testing procedure and the experimental setup. The FRF is measured by increasing the actuation frequency in steps of 10 Hz that provide response curves composed of discrete measured points in the frequency domain; the step width corresponds to the accuracy of the resonance frequency measurement. The second error source is represented by the interferometric microscope sensitivity in detecting vertical motions of the samples; however, its value is nominally 0.1 nm, which is three orders of magnitude lower than the measured oscillation amplitudes and is reasonably negligible. The global error on the quality factor measurements
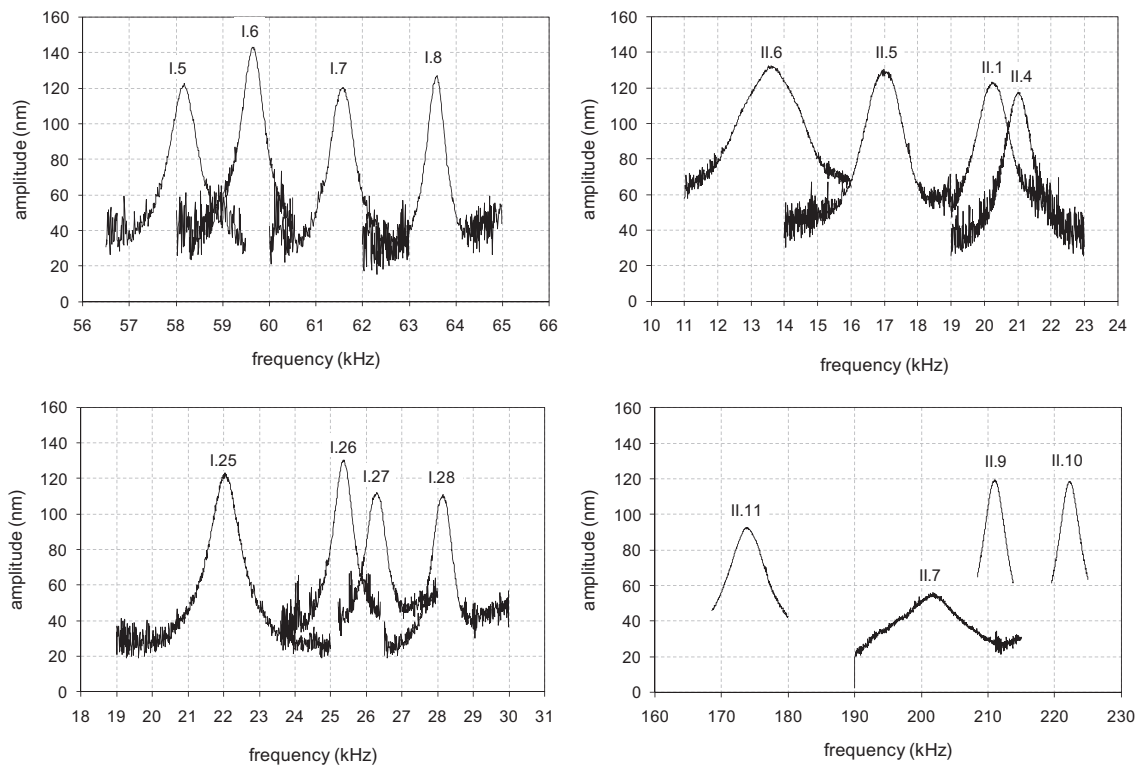
Fig. 9. Experimental FRF of some microstructures; the sample numbers are reported above each curve.
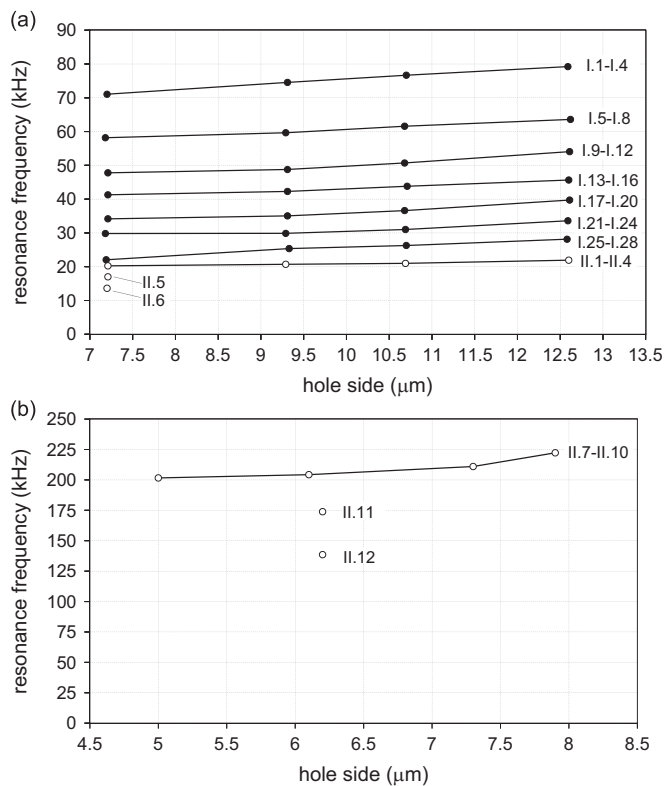

Fig. 10. Measured values of resonance frequency of gold (a) and polysilicon (b) microstructures related to plate and hole dimensions. The black dots refer to typology I (square) and white dots to typology II (rectangular); the sample number is reported near each mark.
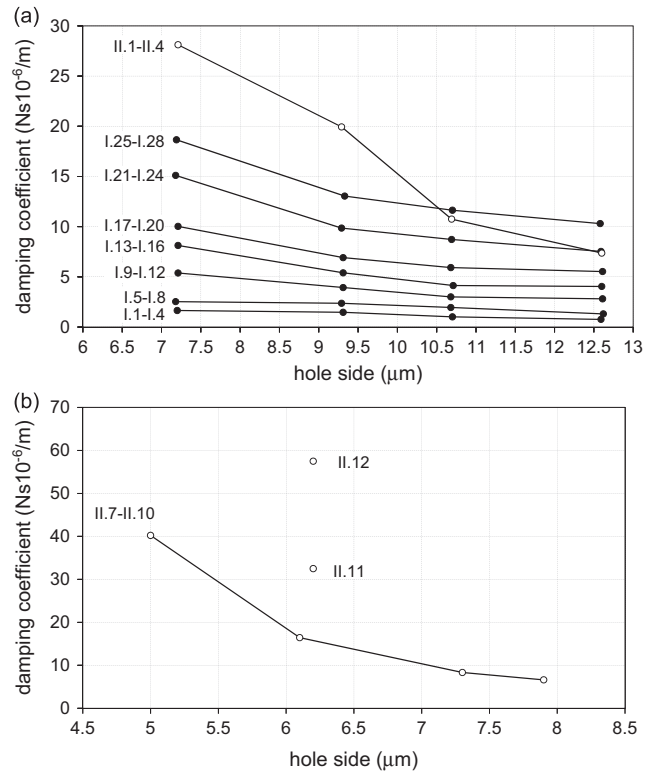
Fig. 11. Measured values of damping coefficient of gold (a) and polysilicon (b) microstructures related to plate and hole dimensions. The black dots refer to typology I (square) and white dots to typology II (rectangular); the sample number is reported near each mark.

Fig. 12. Measured values of quality factor of gold (a) and polysilicon (b) microstructures related to plate and hole dimensions. The black dots refer to typology I (square) and white dots to typology II (rectangular); the sample number is reported near each mark.
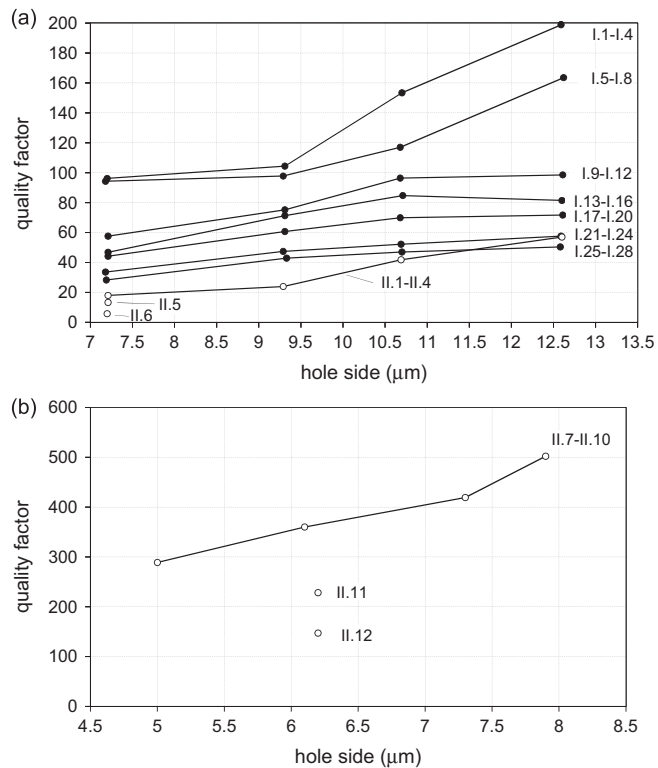
Table 5
Measured values of resonance frequency, half-power bandwidth, damping coefficient, and damping ratio $(100\times)$ of sample I.17 at low air pressures. The mass of the central plate is 20.637×10^{-10} kg.

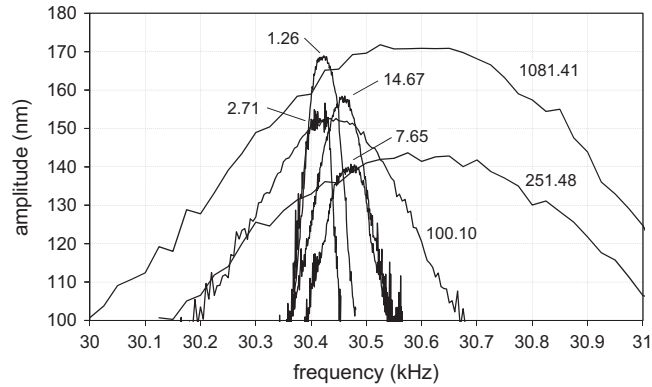| Pressure [mbar]	Resonance frequency f_n [kHz]	Half-power bandwidth Δf_n [kHz]	Damping coefficient c [N s 10^{-6}/m]	Damping ratio ζ [%]
1.26	30.42	0.0892	1.157	0.147
2.71	30.41	0.0821	1.065	0.135
7.65	30.47	0.1548	2.007	0.254
14.67	30.46	0.1543	2.001	0.253
100.10	30.44	0.4258	5.521	0.699
251.48	30.60	0.9233	11.972	1.509
1081.41	30.58	0.9487	12.301	1.551

Fig. 13. Measured FRF of sample I.17 at the different values of environmental air pressures indicated near each curve (unit mbar).
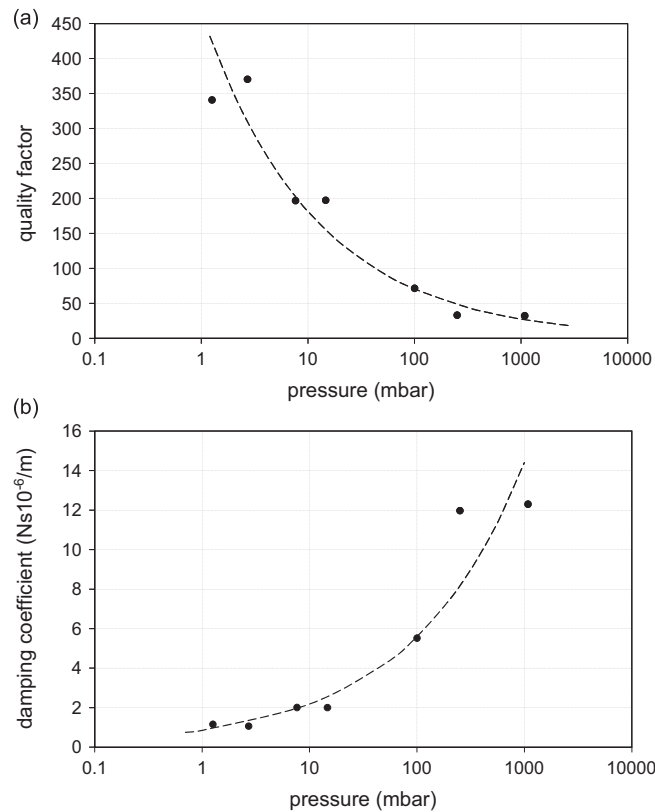

Fig. 14. Experimental values of damping coefficient (a) and quality factor (b) of sample I.17 at variable air pressure.

is estimated in the range between 2.23 and 4.91 percent for gold square samples, between 0.91 and 5.24 percent for rectangular gold samples, and between 0.19 and 0.59 percent for rectangular silicon samples.

6. Conclusion

The optical interferometric technique applied to microstructural experimental analysis produces highly precise detections of the displacement in dynamic conditions. The development of a dedicated algorithm for applying the light interference to microscopy has been discussed with the goal of relating the measured light intensity of fringes to the instant sample position. The experimental setting is completed with the building of the climatic chamber suitable for lowering the environmental air pressure for measurements in rarefied atmosphere. The damping coefficient was estimated through the experimental FRF by means of the half-power method and the measured true geometric dimensions of samples. Samples were designed, built, and prepared for tests with the wire-bonding technique. The parametric variants built allowed investigation of the influence of geometry on viscous dissipations because of the fluid.

This work has the aim of conjugating the different competencies of microsystem designers with those of specialists in optical experimental methods, through the detailed explanation of interferometric microscopy parameters on micro-structural dynamics analysis. Furthermore, the experimental results from measurements on parameterized geometries will represent a useful database for modeling activities in the field of MEMS damping.

Appendix A

By assuming that the two sources of beams described by Eqs. (1) and (2) have the same amplitude, which is

$$E_{10} = E_{20} = E_{i0}, \tag{A1}$$

then the interference wave amplitude becomes

$$E_0 = \sqrt{2E_{i0}^2[1 + \cos(\varphi_1 - \varphi_2)]}. \tag{A2}$$

By using the trigonometric relation $(1 + \cos \alpha)/2 = \cos^2(\alpha/2)$, the last equation can be written as

$$E_0 = \sqrt{4E_{i0}^2 \cos^2\left(\frac{\varphi_1 - \varphi_2}{2}\right)}. \tag{A3}$$

This expression gives the interference wave amplitude produced by the interaction of two coherent light waves with the same amplitude E_{i0} and with the instant phase angles φ_1 and φ_2. The wave amplitude is related to the light intensity I by the equation: $I = E_{i0}^2$. The quantitative detection of light waves can be performed by many different light sensors (e.g., photocells) that are commonly able to read its intensity, making this parameter relevant for interferometric techniques.

When the wave light propagates, the 2π phase angle corresponds to the wave path λ, where λ is the wavelength; then, the generic displacement Δx and the correspondent phase angle variation are related by the following proportionality:

$$\Delta x : \Delta \varphi = \lambda : 2\pi. \tag{A4}$$

Then, the phase shift between the two source waves at the time of collision is directly dependent on their optical paths; if Δx is the optical path difference between the two arms of the interferometer, their phase shift is

$$\varphi_1 - \varphi_2 = \Delta \varphi = \frac{2\pi \Delta x}{\lambda} \tag{A5}$$

and the light intensity of the interference beam is

$$I = 4E_{i0}^2 \cos^2\left(\frac{\pi \Delta x}{\lambda}\right), \tag{A6}$$

which corresponds to Eq. (6). The last relation shows that the interference wave intensity becomes equal to zero (destructive interference) when

$$\frac{\pi \Delta x}{\lambda} = n\frac{\pi}{2}, \quad n = 1, 3, 5, \ldots. \tag{A7}$$

while it reaches its maximum level (constructive interference) when

$$\frac{\pi \Delta x}{\lambda} = n\pi, \quad n = 0, 2, 4, \ldots \tag{A8}$$

The first case corresponds to the OPD

$$\Delta x = n\frac{\lambda}{2}, \quad n = 1, 3, 5, \ldots \tag{A9}$$

and the second case to the OPD

$$\Delta x = n\lambda, \quad n = 1, 3, 5, \ldots. \tag{A10}$$

Starting from Eq. (A2), it is possible to define the intensity as

$$I = 2E_{i0}^2[1 + \cos(\varphi_1 - \varphi_2)] \tag{A11}$$

that can be represented as a generic wave function depending on the phase shift; the visible effect of this function is a sequence of areas, namely, interference fringes, where the light intensity varies as a sinus. The intensity function can be expressed as a sinus variation around the average intensity: by indicating with $I_{\max}$ and $I_{\min}$ the maximum and the minimum light intensities, respectively, it results in

$$I = \frac{I_{\max} + I_{\min}}{2} + \left(\frac{I_{\max} + I_{\min}}{2} - I_{\min}\right)\cos(\varphi_1 - \varphi_2), \tag{A12}$$

where the average intensity can be identified with the ambient light intensity:

$$I_{\mathrm{amb}} = \frac{I_{\max} + I_{\min}}{2}. \tag{A13}$$

By combining Eqs. (A12) and (A13), the intensity becomes

$$I = I_{\mathrm{amb}}[1 + C\cos(\varphi_1 - \varphi_2)], \tag{A14}$$

where the coefficient

$$C = \frac{I_{\mathrm{amb}} - I_{\min}}{I_{\mathrm{amb}}} \tag{A15}$$

represents the fringe contrast. After modifying Eq. (A14) in the following form:

$$I = I_{\mathrm{amb}}[1 + C\cos\{2(\varphi_1 - \varphi_2) - (\varphi_1 - \varphi_2)\}], \tag{A16}$$

the OPD expressed by Eq. (A5) can be introduced to obtain

$$I = I_{\mathrm{amb}}\left[1 + C\cos\left\{\frac{4\pi\Delta x}{\lambda} + \varphi_2 - \varphi_1\right\}\right], \tag{A17}$$

which is the basic form of the algorithm used by the interferometer to relate the OPD to the light intensity detected in static conditions. By introducing a couple of coordinates x,y to identify each pixel on the detector surface and the magnification factor G of the microscope, Eq. (A17) can be written in the final form:

$$I(x,y) = I_{\mathrm{amb}}\left(\frac{x}{G}, \frac{y}{G}\right)\left[1 + C\left(\frac{x}{G}, \frac{y}{G}, \Delta x\right)\cos\left\{\frac{4\pi\Delta x(x/G,\ y/G)}{\lambda_m(1+f)} + \varphi_2\left(\frac{x}{G}, \frac{y}{G}\right) - \varphi_1\right\}\right], \tag{A18}$$

corresponding to Eq. (7), where $(x/G, y/G)$ are the coordinates of the specimen surface corrected with the magnification of the microscope and f is the correction factor dependent on the objective aperture. The wavelength λ has been changed to λ_m representing the average wavelength of the light spectrum.

In case of alternate motion, the OPD is defined as a function of the specimen surface displacement as

$$\Delta x\left(\frac{x}{G}, \frac{y}{G}\right) = \Delta x_0\left(\frac{x}{G}, \frac{y}{G}\right) + a\left(\frac{x}{G}, \frac{y}{G}\right)\sin\left\{\omega t + \Theta\left(\frac{x}{G}, \frac{y}{G}\right)\right\} \tag{A19}$$

where Δx_0 is the average position of the sample, a is the amplitude of oscillation, ω is the angular frequency of the driving force exciting the sample, and Θ is the phase angle between the excitation force and the specimen displacement. By introducing the expression of Eq. (A19) into Eq. (A17) that describes the light intensity variation in static conditions, the following relation is obtained:

$$\begin{aligned}
I(x,y,t) = {} & I_{\mathrm{amb}}\left[1 + C(\Delta x)\cos\left(\frac{4\pi\Delta x_0}{\lambda_{\mathrm{ma}}} + \Delta\varphi\right)J_0\left(\frac{4\pi a}{\lambda_{\mathrm{ma}}}\right)\right] \\
& - 2I_{\mathrm{amb}}C(\Delta x)\sin\left(\frac{4\pi\Delta x_0}{\lambda_{\mathrm{ma}}} + \Delta\varphi\right)J_1\left(\frac{4\pi a}{\lambda_{\mathrm{ma}}}\right)\sin(\omega t + \Theta) \\
& + 2I_{\mathrm{amb}}C(\Delta x)\cos\left(\frac{4\pi\Delta x_0}{\lambda_{\mathrm{ma}}} + \Delta\varphi\right)\sum_{k=1}^{\infty} J_{2k}\left(\frac{4\pi a}{\lambda_{\mathrm{ma}}}\right)\cos(2k(\omega t + \Theta)) \\
& - 2I_{\mathrm{amb}}C(\Delta x)\sin\left(\frac{4\pi\Delta x_0}{\lambda_{\mathrm{ma}}} + \Delta\varphi\right)\sum_{k=1}^{\infty} J_{2k+1}\left(\frac{4\pi a}{\lambda_{\mathrm{ma}}}\right)\sin((2k+1)(\omega t + \Theta))
\end{aligned} \tag{A20}$$

The relation expressed by Eq. (A20) represents the variation of light intensity in dynamic conditions, where

$$\lambda_{ma} = \lambda_m(1 + f), \tag{A21}$$

and J_i are the Bessel functions of order i. Under the hypothesis of oscillation amplitudes being much lower than the objective depth of field and the coherence length, the dependence of C on the OPD can be neglected:

$$C(\Delta x) \cong C(\Delta x_0). \tag{A22}$$

Common light sensors are able to measure the light intensity on each pixel as the average over a determined time interval T_0 (several centimes of a second). This averaged intensity I_m can be expressed with the integral of Eq. (A20) over the

time T_0 divided by the same time interval:

$$I_m(x,y) = \frac{1}{T_0} \lim_{T_0 \to \infty} \int_0^{T_0} I(x,y,t)dt; \tag{A23}$$

by combining Eqs. (A20) and (A23), the following is obtained:

$$I_m(x,y) = I_{\mathrm{amb}}\left[1 + C(\Delta x_0)J_0\left(\frac{4\pi a}{\lambda_{ma}}\right)\cos\left(\frac{4\pi\Delta x_0}{\lambda_{ma}} + \Delta\varphi\right)\right]. \tag{A24}$$

Dynamic Eq. (A24), corresponding to Eq. (10), is the algorithm used by the microscope to convert the light intensity detected by the light sensor to the dynamic displacement of the sample.

References

[1] M. Bao, H. Yang, Y. Sun, P.J. French, Modified Reynolds' equation and analytical analysis of perforated structures, *Journal of Micromechanics and Microengineering* 13 (2003) 795–800.

[2] S.S. Mohite, H. Kesari, V.R. Sonti, R. Pratap, Analytical solutions for the stiffness and damping coefficients of squeeze films in MEMS devices with perforated back plates, *Journal of Micromechanics and Microengineering* 15 (2005) 2083–2092.

[3] T. Veijola, Analytic damping model for an MEM perforation cell, *Microfluidics and Nanofluidics* 2 (2006) 249–260.

[4] T. Veijola, Analytic damping model for a square perforation cell, *Proceedings of the Ninth International Conference on Modeling and Simulation of Microsystems (MSM2006)*, Boston, 2006, pp. 554–557.

[5] A.K. Pandey, R. Pratap, A comparative study of analytical squeeze film damping models in rigid perforated MEMS structures with experimental results, *Microfluidics Nanofluidics* 4 (2008) 205–218.

[6] T. Veijola, A. Lehtovuori, Numerical and analytical modelling of trapped gas in micromechanical squeeze-film dampers, *Journal of Sound and Vibration* 319 (2009) 606–621.

[7] C.L. Berli, A. Cardona, On the calculation of viscous damping of microbeam resonators in air, *Journal of Sound and Vibration* 327 (2009) 249–253.

[8] J.B. Starr, Squeeze-film damping in solid state accelerometers, *Proceedings of IEEE Solid-State Sensor and Actuator Workshop*, Hilton Head Island, 1990, pp. 44–47.

[9] J.E. Mehner, W. Dötzel, B. Schauwecker, D. Ostergaard, Reduced order modeling of fluid structural interactions in MEMS based on modal projection techniques, *Proceedings of Transducers'03*, Boston, 2003, pp. 1840–1843.

[10] R. Sattler, G. Wachutka, Analytical compact models for squeezed-film damping, *Proceedings of Symposium on Design, Test, Integration and Packaging of MEMS/MOEMS (DTIP)*, Montreux, 2004, pp. 377–382.

[11] T. Veijola, Methods for solving gas damping problems in perforated microstructures using a 2D finite-element solver, *Sensors* 7 (2007) 1069–1090.

[12] C. Feng, P. Zhao, D.Q. Liu, Squeeze-film effects in MEMS devices with perforated plates for small amplitude vibration, *Microsystem Technologies* 13 (2007) 623–633.

[13] V. Ostasevicius, R. Dauksevicius, E. Gaidys, A. Palevicius, Numerical analysis of fluid-structure interaction effects on vibrations of cantilever microstructure, *Journal of Sound and Vibration* 308 (2007) 660–673.

[14] G. De Pasquale, T. Veijola, Comparative numerical study of FEM methods solving gas damping in perforated MEMS devices, *Microfluidics and Nanofluidics* 5 (2008) 517–528.

[15] M.M. Altuğ Bıçak, M.D. Rao, Analytical modeling of squeeze film damping for rectangular elastic plates using Green's functions, *Journal of Sound and Vibration* 329 (2010) 4617–4633.

[16] E.S. Kim, Y.H. Cho, M.U. Kim, Effect of holes and edges on the squeeze film damping of perforated micromechanical structures, *Proceedings of IEEE Micro Electro Mechanical Systems Conference (MEMS)*, Orlando, 1999, pp. 296–301.

[17] R. Sattler, G. Wachutka, Compact models for squeeze-film damping in the slip flow regime, *Proceedings of the Seventh International Conference on Modeling and Simulation of Microsystems (MSM2004)*, Boston, 2004, pp. 243–246.

[18] G. Schrag, G. Wachutka, Accurate system-level damping model for highly perforated micromechanical devices, *Sensors and Actuators A* 111 (2004) 222–228.

[19] P.J. Kwok, M.S. Weinberger, K.S. Breuer, Fluid effects in vibrating micromachined structures, *Journal of Microelectromechanical Systems* 14 (2005) 770–781.

[20] G. De Pasquale, A. Somà, Energetic method for non linear dynamic characterization of MEMS squeeze film damping, *Proceedings of 5th European Congress on Computational Methods in Applied Sciences and Engineering (ECCOMAS)*, Venice, 2008.

[21] A. Somà, G. De Pasquale, Numerical and experimental comparison of MEMS suspended plates dynamic behaviour under squeeze film damping effect, *Analog Integrated Circuits and Signal Processing* 57 (2008) 213–224.

[22] T. Veijola, G. De Pasquale, A. Somà, Experimental validation of compact damping models of perforated MEMS devices, *Microsystem Technologies* 15 (2009) 1121–1128.

[23] M. Niessner, G. Schrag, J. Iannacci, G. Wachutka, Macromodel-based simulation and measurement of the dynamic pull-in of viscously damped RF-MEMS switches, *Sensors and Actuators A* 172 (2011) 269–279.

[24] G. De Pasquale, A. Somà, Characterization of damping in vibrating microplates through measurements in the time domain, *Proceedings of Symposium on Design, Test, Integration and Packaging of MEMS/MOEMS (DTIP)*, Cannes, 2012, pp. 76–81.

[25] R. Lifschitz, M.L. Roukes, Thermoelastic damping in micro- and nanomechanical systems, *Physical Review* 61 (2000) 5600–5609.

[26] Y.B. Yi, Geometric effects on thermoelastic damping in MEMS resonators, *Journal of Sound and Vibration* 309 (2008) 588–599.

[27] P. Li, Y. Fang, R. Hu, Thermoelastic damping in rectangular and circular microplate resonators, *Journal of Sound and Vibration* 331 (2012) 721–733.

[28] G. De Pasquale, T. Veijola, A. Somà, Gas damping effect on thin vibrating gold plates: experiments and modeling, *Proceedings of Symposium on Design, Test, Integration and Packaging of MEMS/MOEMS (DTIP)*, Rome, 2009, pp. 23–28.

[29] G. De Pasquale, T. Veijola, A. Somà, Modelling and validation of air damping in perforated gold and silicon MEMS plates, *Journal of Micromechanics and Microengineering* 20 (2010) 015010.

[30] S. Han, T. Browe, Characterizing optically packaged MEMS & MOEMS devices using optical profiling techniques, *Proceedings of the International Symposium on Advanced Packaging Materials: Processes, Properties and Interfaces*, Tucson, 2005, pp. 13–16.

[31] M. Zhou, L. Bai, Z. Li, H. Yao, Measurement of surface profile of microstructure, *Proceedings of SPIE*, 3680 (1999) 863–869.

[32] K. Krupa, C. Gorecki, R. Jozwicki, M. Jozwik, A. Andrei, Interferometric study of reliability of microcantilevers driven by AlN sandwiched between two metal layers, *Sensors and Actuators A* 171 (2011) 306–316.

[33] A. Bosseboeuf, S. Petitgrand, Characterization of the static and dynamic behaviour of M(O)EMS by optical techniques: status and trends, *Journal of Micromechanics and Microengineering* 13 (2003) S23–S33.

[34] S. Petitgrand, R. Yahiaoui, A. Bosseboeuf, K. Danaie, Quantitative time-averaged microscopic interferometry for micromechanical device vibration mode characterization, *Proceedings of the International Symposium on Microelectronics and Micro-Electro-Mechanical Systems (SPIE)*, Adelaide, Vol. 4400 (51), 2001.

[35] G. De Pasquale, A. Somà, Dynamic identification of electrostatically actuated MEMS in the frequency domain, *Mechanical Systems and Signal Processing* 24 (2010) 1621–1633.
[36] G. De Pasquale, M. Barbato, V. Giliberto, G. Meneghesso, A. Somà, Reliability improvement in microstructures by reducing the impact velocity through electrostatic force modulation, *Microelectronics Reliability* 52 (2012) 1808–1811.